Bioinspired PDMS-graphene cantilever flow sensors using 3D printing and replica moulding

Kamat, Amar M; Zheng, Xingwen; Jayawardhana, Bayu; Kottapalli, Ajay Giri Prakash

Published in:
Nanotechnology

DOI:
10.1088/1361-6528/abcc96

Publication date:
2021

PAPER • **OPEN ACCESS**

Bioinspired PDMS-graphene cantilever flow sensors using 3D printing and replica moulding

To cite this article: Amar M Kamat *et al* 2021 *Nanotechnology* **32** 095501

OPEN ACCESS
IOP Publishing
Nanotechnology

Nanotechnology **32** (2021) 095501 (11pp) https://doi.org/10.1088/1361-6528/abcc96

Bioinspired PDMS-graphene cantilever flow sensors using 3D printing and replica moulding

Amar M Kamat[1], **Xingwen Zheng**[1], **Bayu Jayawardhana**[2] and **Ajay Giri Prakash Kottapalli**[1,3]

[1] Advanced Production Engineering, Engineering and Technology Institute Groningen, Faculty of Science and Engineering, University of Groningen, Nijenborgh 4, 9747 AG Groningen, The Netherlands
[2] Discrete Technology and Production Automation, Engineering and Technology Institute Groningen, Faculty of Science and Engineering, University of Groningen, Nijenborgh 4, 9747 AG Groningen, The Netherlands
[3] MIT Sea Grant College Program, Massachusetts Institute of Technology (MIT), 77 Massachusetts Avenue, NW98-151, Cambridge, MA 02139, United States of America

E-mail: a.m.kamat@rug.nl

Received 23 September 2020, revised 29 October 2020
Accepted for publication 20 November 2020
Published 8 December 2020

Abstract

Flow sensors found in animals often feature soft and slender structures (e.g. fish neuromasts, insect hairs, mammalian stereociliary bundles, etc) that bend in response to the slightest flow disturbances in their surroundings and heighten the animal's vigilance with respect to prey and/or predators. However, fabrication of bioinspired flow sensors that mimic the material properties (e.g. low elastic modulus) and geometries (e.g. high-aspect ratio (HAR) structures) of their biological counterparts remains a challenge. In this work, we develop a facile and low-cost method of fabricating HAR cantilever flow sensors inspired by the mechanotransductory flow sensing principles found in nature. The proposed workflow entails high-resolution 3D printing to fabricate the master mould, replica moulding to create HAR polydimethylsiloxane (PDMS) cantilevers (thickness = 0.5–1 mm, width = 3 mm, aspect ratio = 20) with microfluidic channel (150 μm wide × 90 μm deep) imprints, and finally graphene nanoplatelet ink drop-casting into the microfluidic channels to create a piezoresistive strain gauge near the cantilever's fixed end. The piezoresistive flow sensors were tested in controlled airflow (0–9 m s^{-1}) inside a wind tunnel where they displayed high sensitivities of up to 5.8 kΩ m s^{-1}, low hysteresis (11% of full-scale deflection), and good repeatability. The sensor output showed a second order dependence on airflow velocity and agreed well with analytical and finite element model predictions. Further, the sensor was also excited inside a water tank using an oscillating dipole where it was able to sense oscillatory flow velocities as low as 16–30 μm s^{-1} at an excitation frequency of 15 Hz. The methods presented in this work can enable facile and rapid prototyping of flexible HAR structures that can find applications as functional biomimetic flow sensors and/or physical models which can be used to explain biological phenomena.

Supplementary material for this article is available online

Keywords: flow sensing, piezoresistivity, flexible sensors, graphene, 3D printing, bioinspiration

(Some figures may appear in colour only in the online journal)

1. Introduction

Flow sensors found in nature are known to be sensitive to very low fluid velocities as a result of evolutionary design optimization processes operating over millions of years. For instance, the lateral line organ in fishes comprises hair-like cilia structures that can sense oscillatory flow disturbances as low as 18–38 μm s^{-1} [1, 2]. Similarly, sensory thresholds of around 0.1 mm s^{-1} airflow velocity have been reported for the wind-receptor filiform hairs found in crickets [3]. At a higher length scale, seal whiskers have been shown to be sensitive to hydrodynamic stimuli on the order of 245 μm s^{-1} [4]. Such highly optimized and sensitive flow sensors, often present in linear or two-dimensional (2D) arrays, allow the animals to build an accurate three-dimensional (3D) flow map of their surroundings, thus enabling them to perform exquisite tasks such as energy-efficient manoeuvring, object localization, obstacle avoidance, escaping from predators, and tracking prey [5] in conditions that are often noisy and/or murky. Although the flow sensors described above span a large range of length scales (from μm to mm), they often share morphological similarities, most notably, their characteristically high aspect ratios (HARs) (defined as length divided by thickness or diameter of the sensing structure). The flexible HAR structures, e.g. cilia in the fish neuromast (figures 1(a) and (b)), bend easily in response to the drag force caused by flow stimuli, causing afferent neurons at the base of the sensor to fire impulses to the central nervous system and thereby alerting the animal to the tiniest of flow disturbances in its surroundings (figure 1(c)). This simple mechanotransduction sensing principle usually relies upon two major factors for its efficacy: low flexural rigidity of the structure (caused by a combination of low Young's modulus of the sensor material and HAR of the structure) and high innervation density at the base of the sensor.

The field of biomimetic sensors is predicated upon studying, understanding, and applying the sensing principles found in nature to fabricate artificial structures that exploit the optimized biological designs to yield ultrasensitive sensing performance. Specifically, with respect to the flow sensors (e.g. fish neuromasts) discussed above, it is essential for the artificial bioinspired sensors to mimic both the HAR structural design and the softness (i.e. low Young's modulus) of their natural counterparts to create structures with low bending stiffness. The drag force-induced bending strains of the resulting HAR structure are then transduced into a measurable signal using piezoresistive, piezoelectric, capacitive, or optical sensing principles, an example of which is shown in figure 1(d) (piezoresistive flow sensor). Traditionally, bioinspired hair-like flow and tactile sensors have been fabricated using standard microelectromechanical systems (MEMS) fabrication techniques in the cleanroom. Fan *et al* [7] and Chen *et al* [8] used a sensor design comprising a fish-inspired 'cilium' structure located at the distal end of a piezoresistive cantilever, where the drag force-induced bending moment on the cilium was transferred onto the cantilever to generate a measurable change in resistance. In both these works, the MEMS cantilever sensing structure and the vertical cilium were fabricated using surface micromachining and sacrificial etching techniques, requiring the use of cumbersome processes such as plastic deformation magnetic assembly [7, 9] and layer-by-layer spin-coating and patterning of a photosensitive polymer (SU-8) [8] to realize the HAR sensor. Inspired by cricket wind-receptor hairs, Dijkstra *et al* [10] fabricated SU-8 micropillars on suspended Si_xN_y membranes with a capacitive readout using multi-layer deposition and photolithography techniques. Kottapalli *et al* [11] 3D-printed a micropillar and bonded it to a liquid crystal polymer membrane patterned with a serpentine gold strain gauge to realize an all-polymer bioinspired sensor, while Asadnia *et al* [12] used a similar micropillar on a $Pb(Zr_{0.52}Ti_{0.48})O_3$ membrane to fabricate a self-powered piezoelectric sensor. The representative research mentioned above (by no means an exhaustive list) demonstrated the capabilities of sophisticated cleanroom techniques to fabricate arrays of bioinspired HAR flow sensors that displayed sensitivity to both steady-state and oscillatory flow in air and under water. Moreover, the MEMS processes allowed the sensors to be fabricated close to the real scale [10] and yielded threshold detection limits remarkably close to the natural sensors, e.g. 8 μm s^{-1} for an oscillatory stimulus at 35 Hz reported by Asadnia *et al* [12] for their fish-inspired piezoelectric flow sensors. It is also noteworthy that in addition to developing reliable and well-calibrated sensors for engineering applications [13], the bioinspired flow sensors also served as physical models used to generate insights on biological phenomena [14] and/or confirm hypotheses [11], thus reducing the need for animal experiments. However, the above studies also revealed the complexity and tediousness of fabricating the 3D HAR structures using expensive MEMS fabrication methods which were primarily developed by the semiconductor industry for planar (2D) processing of integrated circuits. Further, the limited choice of substrate materials (mainly silicon) available for processing meant that although the geometry of the HAR structures could be replicated fairly accurately, the lab-made bioinspired sensors were much more rigid than the softer hair-like sensors found in nature.

The advent of 3D printing technology with its 'design complexity is free' paradigm has enabled low-cost and facile fabrication of complex biomimetic structures outside the cleanroom. The materials portfolio of 3D printing encompasses a wide variety of polymers, allowing HAR bioinspired sensors to be printed in flexible materials closer to the stiffness of the natural sensors. Moreover, recent advances in flexible electronics have also led to the development and adoption of novel sensing materials such as graphene nanoplatelets (GNP) [15], silver nanoparticle ink [16], liquid metal [17], etc for piezoresistive or capacitive transduction, resulting in much higher sensitivities than conventional materials such as metal strain gauges. However, it must be noted that

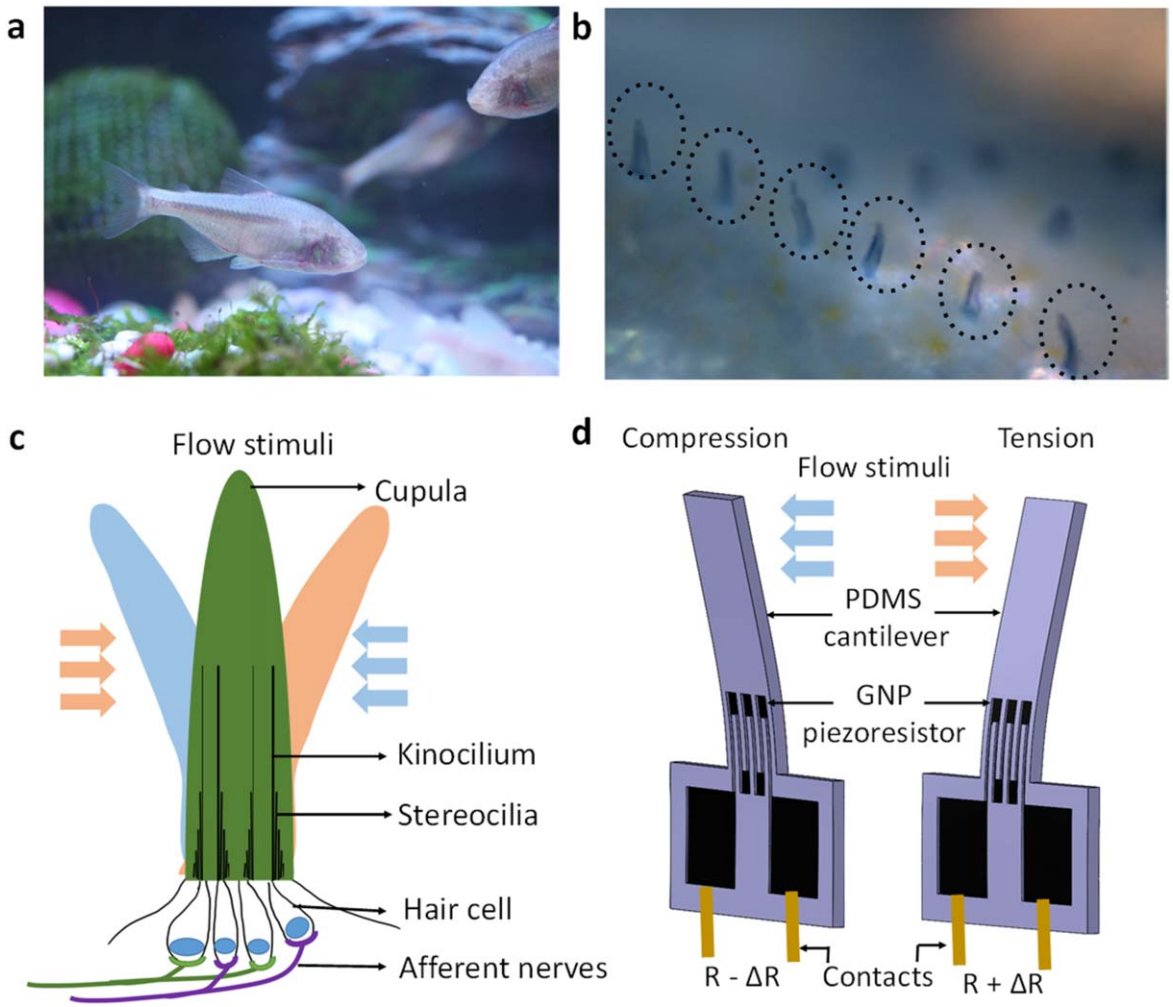

Figure 1. Bioinspiration from fish neuromasts: (a) blind cave fish, (b) fish neuromast sensors (circled) arranged linearly along the lateral line organ, (c) sensing principle of the neuromast sensors comprising HAR hair-like stereocilia bundles encapsulated by a protective gel-like cupula, and (d) bidirectional piezoresisitve cantilever flow sensor inspired by the sensing principle of fish neuromasts. Image b reproduced from [6] with permission. Copyright 2009 Royal Society of Chemistry.

this cleanroom-free fabrication usually comes at the cost of lower resolution and an inability to fabricate at the true scale of the biological sensor when compared to MEMS fabrication techniques. Gul *et al* [18] used multi-material 3D printing to fabricate seal whisker-inspired vortex detection sensors, where the scaled-up whisker-like structure (aspect ratio 20) was printed using polyurethane with graphene strain gauges near its base. Wissman *et al* [17] fabricated a fish-inspired silicone cupula flow sensor with embedded liquid metal capacitors using sacrificial 3D-printed wax moulds. Kamat *et al* [15] developed a cilia-inspired all-polydimethylsiloxane (PDMS) flow/tactile sensor comprising a cilia structure at the distal end of a cantilever with graphene piezoresistors by casting the PDMS structure out of a 3D-printed mould. The group of Krijnen has also recently experimented with direct multi-material 3D printing of flexible whisker-inspired sensors using low-cost extrusion techniques [19, 20]. However, direct 3D printing of soft materials (Young's modulus $\sim 10^3$–10^8 Pa) is still in its early stages of development [21], and fabrication of HAR structures with high-resolution features especially remains a challenge.

In this work, we use a low-cost fabrication process comprising stereolithography (SLA) 3D printing of a replica mould, PDMS casting to form HAR cantilevers with microchannel imprints near its fixed end, and finally GNP drop-casting into the microchannels to realize a bioinspired cantilever flow sensor with piezoresistive sensing elements. Graphene was chosen as the sensing element due to its high gauge factor (GF) [15], mechanical flexibility [22, 23], and simpler integrability into soft polymer structures compared to metal strain gauges. The proposed workflow is compatible with any castable soft polymer and provides a facile route to fabricating soft HAR structures with fine ($\sim$150 μm) features, thus circumventing the problems associated with direct 3D printing of soft materials. We developed a bioinspired HAR cantilever flow sensor featuring PDMS and conductive GNP as the structural and sensing materials, respectively. A detailed characterization of the flow sensor was undertaken by testing it against controlled airflow inside a wind tunnel and controlled oscillatory stimuli inside a water tank. The bioinspired sensor displayed good sensitivity and repeatability in both the airflow (static) and water tank (dynamic) tests, and its

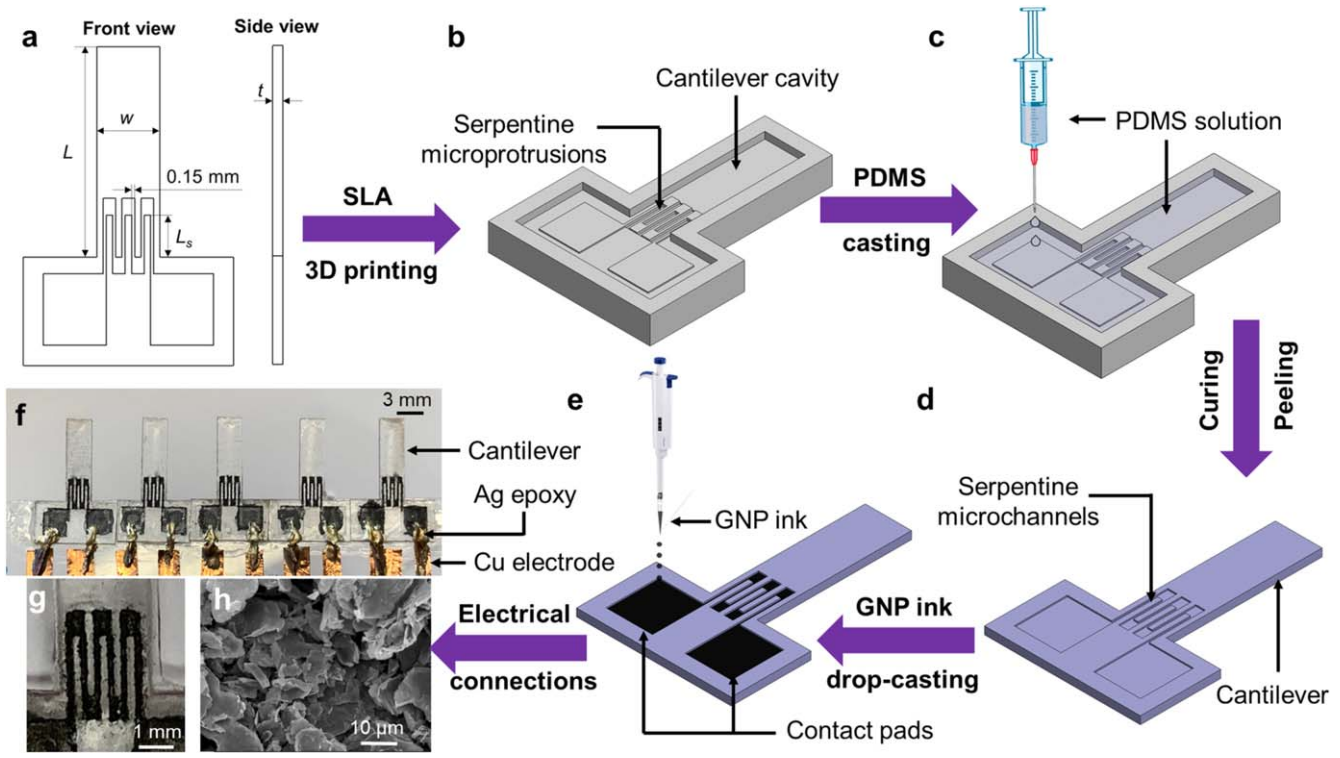

Figure 2. Fabrication processing workflow: (a) cantilever and strain gauge design, (b) SLA 3D-printed mould, (c) PDMS casting inside the mould, (d) cured and peeled PDMS structure, (e) conductive GNP ink drop-casting, (f) photograph (design C2) of five replica-moulded sensors with copper electrodes (scale bar 3 mm), (g) photograph of GNP strain gauge (scale bar 1 mm), and (h) scanning electron (SE) micrograph of graphene nanoplatelets inside microchannels (scale bar 10 μm).

Table 1. Dimensions of two cantilever designs.

	Design parameter	C1	C2
PDMS cantilever	Length, L (mm)	20	10
	Width, w (mm)	3	3
	Thickness, t (mm)	1	0.5
GNP strain gauge	Gauge length, L_s (mm)	2	2
	Microchannel width $\times$ depth (μm $\times$ μm)	150 $\times$ 150	150 $\times$ 90
	Number of serpentine turns	6	6

performance showed good agreement with analytical and finite element method (FEM) models.

2. Experimental details

2.1. Sensor design

The flow sensor was designed as a PDMS cantilever with piezoresistive GNP strain gauges near the fixed end (figure 2(a)). Two cantilever designs were considered, both with an aspect ratio of 20: design C1 which was used in the static wind tunnel tests and design C2 which was used in the dynamic water tank tests with an oscillating sphere. The dimensions of the cantilever and the strain gauge are provided in table 1. The cantilever was attached to a rectangular (10 mm $\times$ 5 mm) fixture for easy handling of the sensors. The fixture featured two square-shaped (3 mm $\times$ 3 mm) contact pads for connections to the electrical circuit.

2.2. Sensor fabrication

The processing workflow used to fabricate the HAR cantilever sensor consisted of a three-step process comprising SLA 3D printing, PDMS replica moulding, and GNP drop-casting, as detailed in the following subsections and in figure 2.

2.2.1. 3D printing of replica mould. SLA, a vat photopolymerization process in which a focused laser beam selectively cures and hardens liquid resin in a layer-by-layer manner [24], was used to 3D-print the replica moulds. The low-cost commercial 3D printer (Formlabs Form 3) used here was equipped with a 250 mW laser (85 μm spot size) and a *XY* (build plane) resolution of 25 μm. We used the 'clear resin' [25] offered by Formlabs to print the moulds since this

material showed the greatest amenability to high-resolution printing of the fine features (~150 μm) required for the GNP strain gauge dimensions. The mould design consisted of a cavity in the shape of the cantilever (figure 2(b)), with serpentine protrusions near the fixed end according to the dimensions given in table 1. The mould was printed such that the cantilever length was along the build direction, since this configuration ensured maximum accuracy in the microchannel dimensions. After printing and removing from the build plate, the mould was washed in isopropyl alcohol (Formlabs Formwash) for 10 min and then UV-cured at 60 °C for 15 min (Formlabs Formcure) per the manufacturer's recommendations to ensure sufficient mechanical strength.

2.2.2. Replica moulding. Commercially available PDMS (Sylgard^{TM} 184) was cast into the moulds (figure 2(c)) to obtain the cantilever structure with microchannel imprints near its fixed end. The two-part PDMS solution was mixed in the ratio (by weight) of 10 parts monomer and 1 part curing agent, mixed thoroughly, degassed inside a vacuum chamber to remove any air bubbles, and finally poured into the moulds using a syringe. The poured solution was evenly spread inside the mould using a doctor's blade and was then cured at 120 °C for 20 min following which the solid PDMS structure was peeled off from the mould (figure 2(d)).

2.2.3. GNP drop-casting. Conductive GNP ink was prepared by mixing commercially obtained (Graphene Supermarket) graphene dispersion (23 wt% graphene concentration, average nanoplatelet thickness ~7 nm) with ethanol in a 1:4 volume ratio. Approximately 10 μl of the diluted ink was drop casted into the square contact pads using a micropipette (figure 2(e)), where it flowed readily into the microchannel via the capillary effect and coated the microchannel walls. The dilution of the GNP dispersion was necessary to improve the flowability of the ink through the microchannels, and the 1:4 dilution ratio mentioned above was found through a series of trials to be enough for the transport of GNP ink in the microchannels via the capillary effect, yielding a consistent base resistance for the sensor. The PDMS/graphene structure was annealed at a temperature of 120 °C for an hour to improve the conductivity of the GNP strain gauge and allow the GNP to form a stable thin film in the microchannel, resulting in a base resistance of approximately 100 ± 10 kΩ. Finally, the sensor fixture was glued to the end of a glass slide (with the cantilever free to move) and the graphene contact pads were connected to copper tapes on the glass slide using conductive silver epoxy (EPOTEK H20E). Optical and scanning electron micrographs of the sensor are shown in figures 2(f)–(h).

2.3. Data acquisition

The copper electrodes from the sensor were connected to a Wheatstone bridge circuit with three fixed resistors of 100 kΩ. The circuit was powered by a 7 V battery and the voltage difference across the bridge was measured using the NI-DAQ USB-6003 data acquisition system. Time series data were recorded in the NI Signal Express 2015 software at a sampling frequency of 2 Hz and 1 kHz for the static and dynamic tests, respectively. The voltage data were converted to resistance data of the sensor using Kirchhoff's laws. For the dynamic tests, the fast Fourier transform (FFT) operation was performed (Origin 2020 software) to convert the time domain data into the frequency domain; the sensor output was then quantified by the height of the FFT peak at the stimulation frequency, assuming the peak existed.

2.4. Sensor testing apparatus

The static airflow testing was conducted using the Aerolab Educational Wind Tunnel with a 305 mm × 305 mm test section. The cantilever flow sensor was mounted vertically in the test section in such a way that the airflow direction was perpendicular to the width plane of the cantilever, and the resistance was continuously monitored for different airflow speeds. For the dynamic tests in water, a vibrating dipole setup (described in detail in [12, 15]) was used to provide the oscillatory stimuli. The sphere (16 mm diameter), driven by a function generator and power amplifier, oscillated at a frequency of 15 Hz where its amplitude could be controlled by changing the voltage input. The sphere amplitude at 15 Hz was calibrated using a Canon EOS 4000D camera equipped with the EF 100 mm macro lens which recorded the oscillation at a sampling frequency of 50 Hz. An open source image processing software (Tracker video analysis [26]) was then used to quantify the oscillation amplitude as a function of input voltage to the function generator.

3. Theory and calculations

The flow sensor bent in response to the streamlined airflow in the wind tunnel which caused a tensile or compressive strain in the GNP strain gauge depending upon whether the airflow impinged on the face containing the strain gauge or the face opposite to the strain gauge. The drag force (F_D) applied by the airflow on the cantilever can be estimated by the well-known drag force equation [27]:

$$F_D = \frac{C_D \times \rho \times w \times L \times U^2}{2}, \tag{1}$$

where C_D is the drag force coefficient, ρ is the density of air, w and L refer to the width and length of the cantilever, respectively, and U is the airflow velocity in the wind tunnel. We seek the average strain induced in the strain gauge by the drag force F_D on the cantilever. To this end, we invoke the flexure formula [28], relating the bending stress at the cantilever surface ($\sigma(x)$) to the internal bending moment ($M(x)$) developed in the cantilever due to the drag force, as:

$$\sigma(x) = \frac{M(x) \times \left(\frac{t}{2}\right)}{I}, \tag{2}$$

where t is the thickness of the cantilever, I is the area moment of inertia about the bending (neutral) axis, and x is the coordinate defined along the length of the cantilever ($x = 0$ at

the fixed end and $x = L$ at the free end). For a rectangular cross-section, the area moment of inertia is given by $I = \frac{w \times t^3}{12}$. The drag force represents a uniformly distributed load on the cantilever and can be shown [28] to cause a bending moment of:

$$M(x) = \frac{F_D \times (L - x)^2}{2 \times L}. \tag{3}$$

Finally, using Hooke's law, we can relate the strain ($\varepsilon(x)$) to the stress as:

$$\varepsilon(x) = \frac{\sigma(x)}{E}, \tag{4}$$

where E is the Young's modulus of the cantilever material. Combining the above equations, we obtain:

$$\varepsilon(x) = \frac{3 \times C_D \times \rho \times (L - x)^2 \times U^2}{2 \times E \times t^2} \tag{5}$$

which represents the surface strain profile along the length of the cantilever as a function of the airflow velocity U. Since the GNP strain gauge is of a finite length (equal to the 'gauge length' L_s), the average strain sensed by the strain gauge (ε_{SG}) can be assumed to be the average of $\varepsilon(x)$ from $x = 0$ to L_s (neglecting the finite depth of the microchannels):

$$\varepsilon_{SG} = \frac{1}{L_s} \int_0^{L_s} \varepsilon_{(x)} dx. \tag{6}$$

Evaluating the simple integral in (6), we arrive at the relation between the strain sensed by the GNP strain gauge and the airflow velocity as:

$$\varepsilon_{SG} = \frac{3 \times C_{D\times}\rho \times (L^2 - LL_s + L_s^2/3) \times U^2}{2 \times E \times t^2}. \tag{7}$$

Conductive GNP is piezoresistive in nature due to the ability of neighbouring nanoplatelets to easily slide over each other upon the application of mechanical strain [29]. Thus, the strain (given by (7)) in the strain gauge grooves causes a resistance change in the GNP conductive path. The fractional change in resistance of the strain gauge can be related to the average strain ε_{SG} using the concept of the GF which is defined as the ratio of the fractional change of resistance to the strain:

$$G = \frac{\Delta R}{\varepsilon_{SG} \times R_{GL,0}}, \tag{8}$$

where G is the GF (assumed to be constant here) of the GNP-on-PDMS strain gauge for static wind tunnel tests, ΔR is the change in resistance of the strain gauge, and $\Delta R_{GL,0}$ is the initial (at rest) resistance of the gauge length of the strain gauge. The conductive path of the strain gauge (from one contact pad to another) is comprised of several resistors arranged in series whose individual resistances depend upon their respective widths (inverse proportionality) and lengths (direct proportionality). It can be easily shown from the geometry of the strain gauge (table 1 and figure 2(a)) that the base resistance of the gauge length portion of the strain gauge ($\Delta R_{GL,0}$) is 0.83 times the total base resistance of the strain gauge (R_0), the latter being the value that is actually measured in the experiment. Taking this into account and combining (7) and (8), the analytical model developed above predicts the piezoresistive sensor output as a function of airflow velocity as:

$$\frac{\Delta R}{R_0} = \frac{1.245 \times G \times C_D \times \rho \times (L^2 - LL_s + L_s^2/3)}{E \times t^2} \times U^2. \tag{9}$$

Equation (9) allows us to predict, at least qualitatively, the effect of design parameters on the performance of the sensor, addition information is provided in the supplementary material S1 (available online at stacks.iop.org/NANO/32/095501/mmedia). The values used for the parameters in (9) are given in table 2.

Table 2. Values of parameters used in analytical model.

Parameter	Value
G	35 [15]
C_D	1.17 [27]
ρ (at 20 °C)	1.2 kg m^{-3} [27]
L	20 mm
L_s	2 mm
E	2.5 MPa [30, 31]
t	1 mm

4. Results and discussion

4.1. Static airflow testing

The cantilever flow sensor (design C1) was positioned vertically in the middle of the test section of the wind tunnel (figure 3(a)). The airflow impinged upon the face opposite to that containing the strain gauge so that the compressive strain was induced in the strain gauge; this was a deliberate choice since the GNP strain gauge output was found to be more stable in the compressive state than in the tensile state in preliminary tests. The airflow velocity in the wind tunnel was first ramped up from 0 to 9.2 m s^{-1} in steps of approximately 0.9 m s^{-1} and then ramped down from 9.2 to 0 m s^{-1} in the reverse order, with a hold of 1 min at each velocity. The sensor resistance was monitored continuously throughout the test. Six such ramp-up and ramp-down tests, each of which lasted for 21 min, were conducted, and the average fractional resistance change at each velocity was recorded to construct a calibration curve (figure 3(b)). The calibration curve indicates a hysteretic response characteristic of viscoelastic elastomers such as PDMS. The maximum hysteresis (at 5.1 m s^{-1} airflow speed) was calculated to be 11% of the full-scale defection. Further, the sensor displayed good repeatability (average $\Delta R = 12.7 \pm 1$ kΩ) in 15 cyclic tests (figure 3(c)) where each cycle consisted of the wind tunnel being turned on for 30 s (air flow speed 4 m s^{-1}) and then turned off for 30 s. Viscoelastic creep deformation [32] of the elastomeric PDMS caused a drift of ~2% in the baseline resistance over the course of the cyclic testing, as seen in figure 3(c).

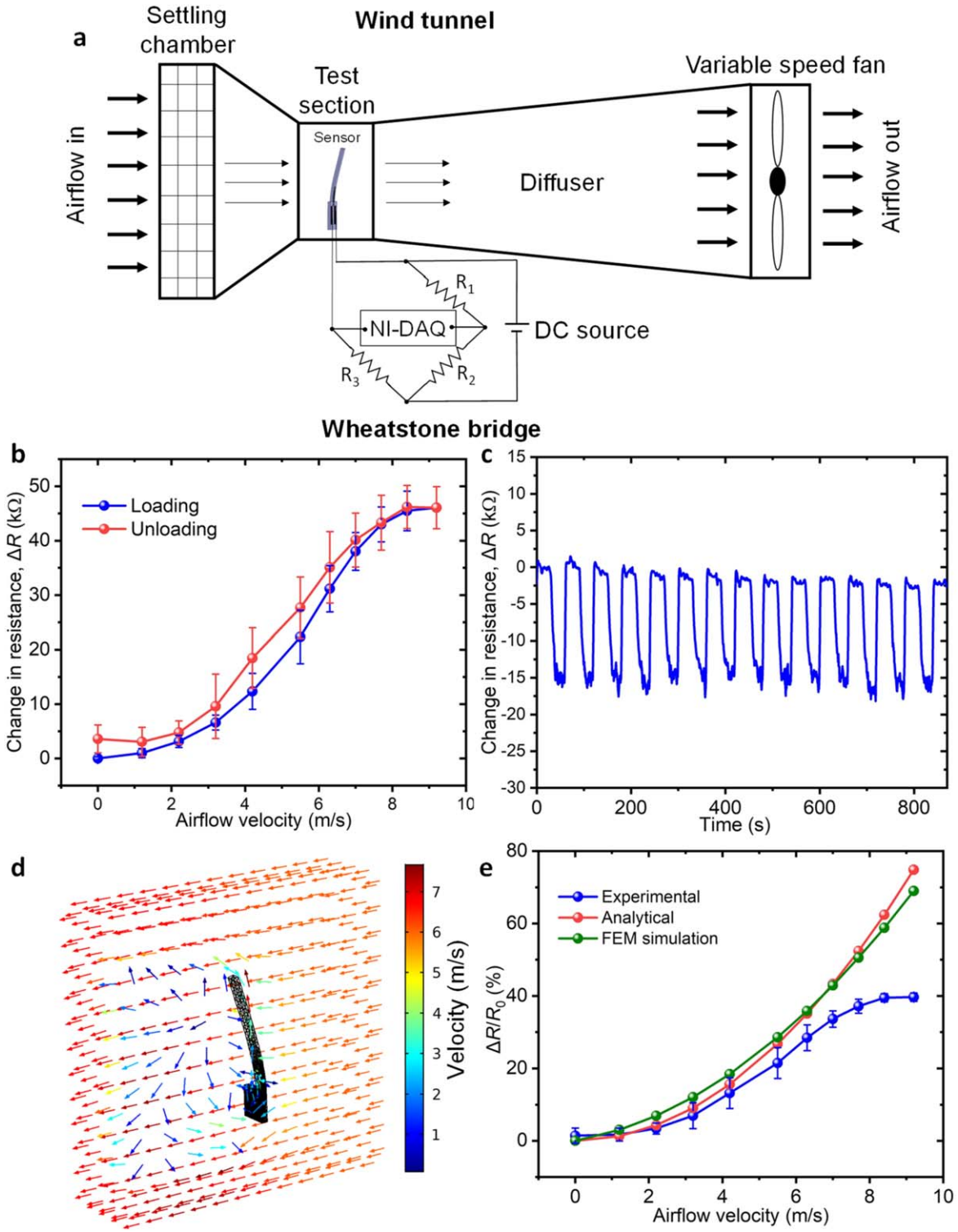

Figure 3. Static airflow testing in wind tunnel: (a) test schematic, (b) calibration curve showing hysteresis, (c) repeatability test for a periodic airflow stimulus of 4.2 m s^{-1} (hold period 30 s in both the ON and OFF states), (d) steady-state FEM fluid-structure interaction simulation showing 3D flow field causing cantilever bending, and (e) comparison of experimental results with analytical and FEM model predictions of fractional resistance change.

The loading and unloading sections of the calibration curve were averaged and compared to the predictions of the analytical model expressed in (9). Further, a 3D FEM model was also developed using the COMSOL Multiphysics® software to verify the analytical model, as shown in figure 3(d). The coupled fluid mechanics-structural mechanics module of the software was used to simulate the fluid-structure interaction (FSI) between the airflow and the flexible cantilever structure in a stationary study (i.e. steady-state conditions) using laminar flow models. Detailed information

regarding the simulation domain, meshing, and boundary conditions used in the FEM model are provided in the supplementary material (S2). The strain inside the gauge length of the microchannel grooves was measured by computing the fractional increase in length of a predefined line (initial length $= L_s$) inside each of the six microchannels comprising the strain gauge, which provided the average bending strain inside the GNP strain gauge. The model predictions (both analytical and FEM) agreed very well with the measured piezoresistive sensor output (figure 3(e)) up to a velocity of around 5.1 m s^{-1}, with both the experimental and numerical resistance change data showing a parabolic dependence on the airflow velocity. The quadratic relation between the piezoresistive sensor output and the airflow velocity has been observed before in the literature [33]. At airflow velocities greater than 5.1 m s^{-1}, the sensor output deviated away from the parabolic prediction and saturated at higher velocities of ~9 m s^{-1}. Although the analytical model developed in section 3 contained many simplifying assumptions such as using: (i) a linear elastic material model for PDMS, (ii) the Euler–Bernoulli theory which usually is valid only for very small beam rotations, (iii) a constant drag force coefficient over the entire flow velocity range (Reynold's number ~12 200 at the highest speed of 9.2 m s^{-1}), and (iv) a constant GF (i.e. no dependence of the GF on the applied strain), it is noteworthy that the model was still able to predict the experimental result well till medium velocities. Since the FEM model did not explicitly make assumptions (i)–(iii) above and yet matched well with the analytical model, it is reasonable to conclude that the sensor output saturation was caused by a decrease in the GF at greater values of bending strain caused by the higher airflow velocities. This conclusion, however, needs to be substantiated in future studies by calibrating the cantilever sensor against controlled bending loads to quantify the variation of the GF with different bending deformations. The analytical model can thus be used to tune the design parameters in order to achieve sensitivity in a desired flow velocity range.

In general, the performance of the sensor compared favourably with similar cantilever sensors reported in the literature. For instance, Kaidarova *et al* [34] fabricated a serpentine laser-induced graphene strain gauge on a flexible polyimide cantilever of comparable dimensions (15 mm × 7 mm × 0.125 mm). The GF they reported was 11 which was around a third of the GNP-on-PDMS GF (35 [15]) used in this work. Consequently, the piezoresistive sensitivity to airflow found in this study (~5800 Ω m s^{-1}) was more than 50 times that reported by Kaidarova *et al* [34]. Moreover, it must be noted that they reported the sensitivity of the flow sensor for water flow which is always greater than the sensitivity to airflow, since the drag force exerted by a fluid on the cantilever is proportional to the density of the fluid, and water is around 800 times denser than air. Further, the maximum hysteresis reported here (11% F.S.) was lower than that reported by Ma *et al* [35] for their bent cantilever flow sensors (20% F.S.). In general, a trade-off between hysteresis and high sensitivity can be recognized in soft polymer sensors, and properly optimized material choices, fabrication processes, and models accounting for polymer creep [36] can be potential strategies to minimize hysteresis errors in sensor output. Further, the piezoresistive sensor also displayed sensitivity to ambient temperature (details given in Supplementary Material S3) with a temperature coefficient of resistance of ~0.014/°C which was of the same order of magnitude as that reported for GNP previously in the literature [37], suggesting the need for temperature compensation strategies to reduce sensor drift during operation.

4.2. Dynamic waterflow testing

The cantilever sensor (design C2) was subjected to dynamic stimuli generated in water using a sphere oscillating at 15 Hz. The oscillating sphere stimulus is routinely used in the fish biology literature (both in experiments with real fish [38] and fish-inspired sensors [12]) to study how the fish neuromast sensors in the lateral line organ are able to sense flow disturbances, since the pulsating 'dipole' flow field is similar to that generated by swimming fish and zooplankton in the real marine environment [5]. The dynamic water tests were conducted in a water tank for different stimulus intensities by changing the dipole vibration amplitude and the distance between the dipole source and the cantilever sensor. The cantilever was fixed approximately 10 mm away from the wall of the water tank, and since the GNP strain gauge was exposed to the environment, only half of the cantilever was vertically dipped into the water to avoid the GNP from contacting the water. The sphere vibrated with an amplitude A and was placed at a distance d (measured from the centre of the sphere) away from the cantilever (figure 4(a)). The calibration of the dipole (figure 4(b)) allowed us to precisely vary the dipole amplitude based on the input voltage. The sphere vibrated along the vertical direction and its topmost point lay approximately 1 mm below the water surface in the rest position. Two tests were conducted: (i) varying A from 0 to 0.28 mm keeping $d = 25$ mm constant, and (ii) varying d from 15 to 100 mm while keeping $A = 0.28$ mm constant. Figure 4(c) shows a comparison of the sensor response (raw data in the time domain) with and without the sphere oscillation at 15 Hz for a representative case of $A = 0.28$ mm and $d = 15$ mm. The sensor output was defined as the FFT resistance peak at 15 Hz based on three experiments, each lasting up to 450 cycles of sphere oscillation.

Figure 4(d) shows the effect of varying the sphere-cantilever distance (d) on the sensor response. The sensor output was strong ($833 \pm 15\ \Omega$) at shorter distances (less than ~25 mm) and decreased rapidly with increasing distances, asymptotically approaching zero at large distances. Surprisingly, the sensor output displayed a discernible local minimum (figure 4(d)) at a sphere-cantilever distance of 20 mm. This dip in the sensor output at $d = 20$ mm was unexpected and was hypothesized to be due to edge effects caused by the proximity of the sensor to the water tank wall (10 mm) and the sphere to the water surface (1 mm from the top of the sphere). To investigate further, a 2D time-dependent FEM model was created using COMSOL® Multiphysics to simulate the FSI between the oscillating sphere and the PDMS

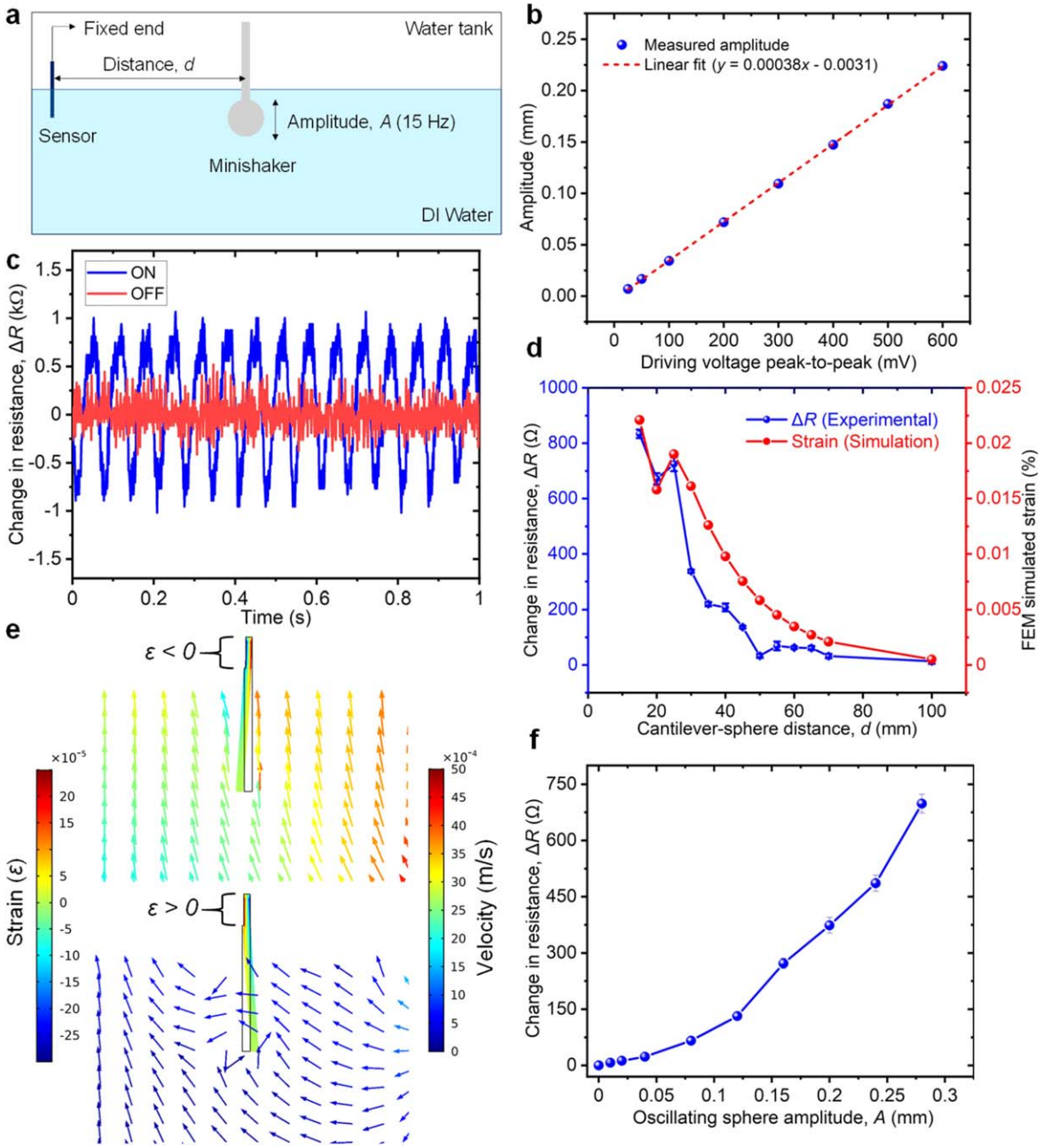

Figure 4. Dynamic flow testing in water tank: (a) test schematic defining A and d, (b) dipole calibration, (c) an example of the sensor response to the 15 Hz stimulus, (d) sensor output as a function of varying distance (d) showing the local minimum at $d = 20$ mm, (e) 2D FEM simulation showing flow field and oscillatory strain in the cantilever (animation available as video S5 in the Supplementary Material), and (f) sensor output as a function of varying sphere amplitude (A) at 15 Hz.

cantilever. The air-water interface was modelled using the 'stationary free surface' boundary condition, while the solid-fluid interfaces were modelled using standard 'no slip' boundary conditions. Other pertinent details of the model are available in the supplementary material (S4). The FSI model confirmed that the cantilever oscillated in response to the dipole flow field (figure 4(e)), with the cantilever groove experiencing compressive and tensile stresses periodically at the same frequency as that of the oscillating sphere (i.e. 15 Hz). An animation of the time-dependent FSI simulation can be found in the Supplementary Material (video S5). Simulations were conducted wherein d was varied from 15 to 100 mm similar to the experiments, and the average strain in the cantilever groove (computed as the FFT peak at 15 Hz of the y-component of the simulated time-varying strain) was calculated in COMSOL®. Interestingly, the simulation results (figure 4(d)) confirmed the local minimum in the cantilever strain, thus mirroring the experimental observation. When the distance between the cantilever and the left wall and between the sphere and the free water surface was increased (to 60 and 75 mm, respectively) in the FEM model, the local minimum in the strain-distance curve disappeared, indicating that the dip in the sensor output was indeed a consequence of edge effects caused by standing waves between the pressure wave

generator (sphere) and reflectors (left wall and free surface). Further, the sensor showed a non-zero output (i.e. a discernible FFT peak at 15 Hz) for the longest tested distance of 100 mm, corresponding to a root mean square (rms) fluid velocity of $\sim$30 μm s^{-1} perpendicular to the cantilever (estimated using the FEM model) near the sensor tip.

Finally, figure 4(e) shows the sensor response to varying sphere oscillation amplitudes. The output was second-order with respect to the oscillating sphere amplitude, agreeing with similar dipole tests conducted on bioinspired flow sensors in the literature [12, 15]. The sensor was sensitive to the lowest oscillating amplitude of 0.01 mm corresponding to an estimated rms flow velocity of $\sim$16 μm s^{-1} perpendicular to the cantilever near the sensor tip. The sensor thus displayed oscillatory velocity sensing thresholds as low as 16–30 μm s^{-1} at 15 Hz, which is comparable to the range (18–38 μm s^{-1} at 10–20 Hz) reported for fish flow receptors in the literature [1, 2].

5. Summary and conclusions

In this work, we presented a low-cost processing workflow to fabricate bioinspired piezoresistive cantilever flow sensors using SLA 3D printing and replica moulding. The resulting sensor structures emulated both the softness ($\sim$2.5 MPa) and HARs ($\sim$20) of the natural flow receptors found in fishes and insects. Further, using conductive GNP ink as the sensing material for the strain gauge near the fixed end of the cantilever, we realized a piezoresistive flow sensor that was tested against both static (air) and dynamic (water) stimuli. The sensor showed excellent sensitivity (5800 Ω m s^{-1}), low hysteresis (11% F.S.), and good repeatability in the static airflow tests. The sensor output was found to be quadratic with respect to airflow velocity till $\sim$5 m s^{-1} (showing excellent agreement with analytical and FEM model predictions) after which it saturated. In the dynamic tests conducted in water, the sensor was able to respond to rms velocities as low as 16–30 μm s^{-1} at an excitation frequency of 15 Hz generated by an oscillating sphere, matching the performance of actual fish neuromast sensors found in nature. Moreover, the sensor was able to detect a local minimum in the flow field of the oscillating sphere (at a distance of 20 mm away from it) caused by edge effects in the finite-sized water tank.

The experimental and analytical methodologies developed in this work can be used to design and fabricate soft polymeric and HAR flow sensors in a facile manner outside the cleanroom. In contrast with traditional approaches of fabricating bioinspired flow sensors using standard MEMS fabrication techniques, the proposed workflow of 3D printing and replica moulding is cheaper, quicker, and offers more flexibility with respect to the choice of structural and sensing materials. Moreover, fabrication of linear arrays of cantilever sensors (e.g. to build sensing systems inspired by the fish lateral line) can be realized easily by changing the mould design to include multiple cantilever cavities. Further, recent trends towards miniaturization in 3D printing (e.g. micro-stereolithography [39]) offer exciting opportunities to scale down the sensor dimensions to truly mimic the size, shape, mechanical properties, and functionality of natural hair-like sensors. Such artificial bioinspired sensors can be used either as functional sensors for flow measurements or to construct physical models in order to understand and explain biological phenomena.

Acknowledgments

This work was labelled by ITEA and funded by local authorities under the grant agreement ITEA-2018-17030-Daytime. The authors gratefully acknowledge Mr David Veninga (University of Groningen) for his assistance with FEM modelling, Dr Gerard Schepers and Mr Wouter Swart Ranshuysen (Hanze University of Applied Sciences) for their help with wind tunnel testing, and Professor Michael Triantafyllou (Massachusetts Institute of Technology) for helpful discussions regarding interpretation of the dipole test results.

ORCID iDs

Amar M Kamat https://orcid.org/0000-0002-1622-9067
Ajay Giri Prakash Kottapalli https://orcid.org/0000-0002-3868-7069

References

[1] Kroese A B A, der Zalm J M and den Bercken J 1978 Frequency response of the lateral-line organ of xenopus laevis *Pflügers Arch.* **375** 167–75
[2] Coombs S and Jansse J 1989 Peripheral processing by the lateral line system of the Mottled Sculpin (Cottus bairdi) BT —the mechanosensory lateral line *The Mechanosensory Lateral Line* ed S Coombs *et al* (New York, NY: Springer New York) pp 299–319
[3] Shimozawa T, Murakami J and Kumagai T 2003 Cricket wind receptors: thermal noise for the highest sensitivity known *Sensors and Sensing in Biology and Engineering* ed F G Barth *et al* (Vienna: Springer Vienna) pp 145–57
[4] Dehnhardt G, Mauck B and Bleckmann H 1998 Seal whiskers detect water movements *Nature* **394** 235–6
[5] Triantafyllou M S, Weymouth G D and Miao J 2016 Biomimetic survival hydrodynamics and flow sensing *Annu. Rev. Fluid Mech.* **48** 1–24
[6] McConney M E, Chen N, Lu D, Hu H A, Coombs S, Liu C and Tsukruk V V 2009 Biologically inspired design of hydrogel-capped hair sensors for enhanced underwater flow detection *Soft Matter* **5** 292–5
[7] Fan Z, Chen J, Zou J, Bullen D, Liu C and Delcomyn F 2002 Design and fabrication of artificial lateral line flow sensors *J. Micromech. Microeng.* **12** 655–61
[8] Chen N, Tucker C, Engel J M, Yang Y, Pandya S and Liu C 2007 Design and characterization of artificial haircell sensor for flow sensing with ultrahigh velocity and angular sensitivity *J. Microelectromech. Syst.* **16** 999–1014
[9] Zou J, Chen J, Liu C and Schutt-Aine J E 2001 Plastic deformation magnetic assembly (PDMA) of out-of-plane microstructures: technology and application *J. Microelectromech. Syst.* **10** 302–9

[10] Dijkstra M, van Baar J J, Wiegerink R J, Lammerink T S J, de Boer J H and Krijnen G J M 2005 Artificial sensory hairs based on the flow sensitive receptor hairs of crickets *J. Micromech. Microeng.* **15** S132–8
[11] Kottapalli A G P, Asadnia M, Miao J and Triantafyllou M 2014 Touch at a distance sensing: lateral-line inspired MEMS flow sensors *Bioinspir. Biomim.* **9** 46011
[12] Asadnia M, Kottapalli A G P, Miao J, Warkiani M E and Triantafyllou M S 2015 Artificial fish skin of self-powered micro-electromechanical systems hair cells for sensing hydrodynamic flow phenomena *J. R. Soc. Interface* **12** 20150322
[13] Asadnia M, Kottapalli A G P, Haghighi R, Cloitre A, Alvarado P V Y, Miao J and Triantafyllou M 2015 MEMS sensors for assessing flow-related control of an underwater biomimetic robotic stingray *Bioinspir. Biomim.* **10** 36008
[14] Casas J, Steinmann T and Krijnen G 2010 Why do insects have such a high density of flow-sensing hairs? Insights from the hydromechanics of biomimetic MEMS sensors *J. R. Soc. Interface* **7** 1487–95
[15] Kamat A M, Pei Y and Kottapalli A G P 2019 Bioinspired cilia sensors with graphene sensing elements fabricated using 3D printing and casting *Nanomaterials* **9** 954
[16] Wu S Y, Yang C, Hsu W and Lin L 2015 3D-printed microelectronics for integrated circuitry and passive wireless sensors *Microsyst. Nanoeng.* **1** 1–9
[17] Wissman J P, Sampath K, Freeman S E and Rohde C A 2019 Capacitive bio-inspired flow sensing cupula *Sensors* **19** 2639
[18] Gul J Z, Su K Y and Choi K H 2018 Fully 3D printed multi-material soft bio-inspired whisker sensor for underwater-induced vortex detection *Soft Robot.* **5** 122–32
[19] Delamare J, Sanders R and Krijnen G 2016 3D printed biomimetic whisker-based sensor with co-planar capacitive sensing *2016 IEEE SENSORS* pp 1–3
[20] Eijking B, Sanders R and Krijnen G 2017 Development of whisker inspired 3D multi-material printed flexible tactile sensors *2017 IEEE SENSORS* pp 1–3
[21] Zhou L-Y, Fu J and He Y 2020 A review of 3D printing technologies for soft polymer materials *Adv. Funct. Mater.* **30** 2000187
[22] Song R *et al* 2018 Flexible graphite films with high conductivity for radio-frequency antennas *Carbon* **130** 164–9
[23] Wang Z *et al* 2020 High conductive graphene assembled films with porous micro-structure for freestanding and ultra-low power strain sensors *Sci. Bull.* **65** 1363–70
[24] Melchels F P W, Feijen J and Grijpma D W 2010 A review on stereolithography and its applications in biomedical engineering *Biomaterials* **31** 6121–30
[25] Formlabs 2017 Clear resin technical data https://formlabs-media.formlabs.com/datasheets/Clear_Resin_Technical.pdf
[26] Brown D 2020 Tracker Video Analysis https://psrc.aapt.org/items/detail.cfm?ID=1970
[27] White F M 2011 *Fluid Mechanics* (New York: McGraw-Hill)
[28] Hibbeler R C 2011 Bending *Mechanics of Materials* 8th (USA: Pearson Prentice Hall) 60-13-602230-8
[29] Hempel M, Nezich D, Kong J and Hofmann M 2012 A novel class of strain gauges based on layered percolative films of 2D materials *Nano Lett.* **12** 5714–8
[30] Wang Z, Volinsky A A and Gallant N D 2014 Crosslinking effect on polydimethylsiloxane elastic modulus measured by custom-built compression instrument *J. Appl. Polym. Sci.* **131** 1–4
[31] Johnston I D, McCluskey D K, Tan C K L and Tracey M C 2014 Mechanical characterization of bulk Sylgard 184 for microfluidics and microengineering *J. Micromech. Microeng.* **24** 035017
[32] Pethrick R A 2010 *Polymer Science and Technology: For Engineers and Scientists* (Caithness, UK: Whittles Publishing)
[33] Aiyar A R, Song C, Kim S H and Allen M G 2009 An all-polymer airflow sensor using a piezoresistive composite elastomer *Smart Mater. Struct.* **18** 115002
[34] Kaidarova A *et al* 2019 Wearable multifunctional printed graphene sensors *npj Flex. Electron.* **3** 1–10
[35] Ma R H, Wang D A, Hsueh T H and Lee C Y 2009 A MEMS-based flow rate and flow direction sensing platform with integrated temperature compensation scheme *Sensors* **9** 5460–76
[36] Sundin J, Kokmanian K, Fu M K, Bagheri S and Hultmark M 2020 A soft material flow sensor for micro air vehicles *Soft Robot.* **00** 1–9
[37] Tian M, Huang Y, Wang W, Li R, Liu P, Liu C and Zhang Y 2014 Temperature-dependent electrical properties of graphene nanoplatelets film dropped on flexible substrates *J. Mater. Res.* **29** 1288–94
[38] Goulet J, Engelmann J, Chagnaud B P, Franosch J M P, Suttner M D and Van Hemmen J L 2008 Object localization through the lateral line system of fish: theory and experiment *J. Comp. Physiol.* A **194** 1–17
[39] You S, Miller K and Chen S 2019 Microstereolithography *Biofabrication and 3D Tissue Modeling* (*Biomaterials Science Series*) (London, UK: The Royal Society of Chemistry) pp 1–21978-1-78801-198-3